The Astrophysical Journal, 921:135 (8pp), 2021 November 10 https://doi.org/10.3847/1538-4357/ac1fe7

Ion Acceleration and the Development of a Power-law Energy Spectrum in Magnetic Reconnection

H. Che[1,2], G. P. Zank[1,2], and A. O. Benz[3,4]
[1] Center for Space Plasma and Aeronomic Research (CSPAR), University of Alabama in Huntsville, Huntsville, AL 35805, USA; hc0043@uah.edu
[2] Department of Space Science, University of Alabama in Huntsville, Huntsville, AL 35899, USA
[3] University of Applied Sciences and Arts Northwestern Switzerland (FHNW), CH-5210 Windisch, Switzerland
[4] Institute for Particle Physics and Astrophysics, ETH Zürich, 8093, Zürich, Switzerland
Received 2021 June 17; revised 2021 August 19; accepted 2021 August 19; published 2021 November 9

Abstract

How charged particles are accelerated efficiently and form a power-law energy spectrum in magnetic reconnection is a problem that is not well understood. In a previous paper, it was shown that the electron Kelvin–Helmholtz instability (EKHI) in force-free magnetic reconnection generates fast-expanding vortices that can accelerate electrons in a few tens of ion gyroperiods (less than 1 ms in the solar corona) to form a power-law energy distribution. In this paper, we present a particle-in-cell (PIC) simulation study of ion acceleration in force-free magnetic reconnection in the presence of the EKHI-induced turbulence. We find that ions are not significantly accelerated by the EKHI-induced stochastic electric field until the magnetic vortices expand to sizes comparable to the ion gyroradius. The Alfvén waves generated by the EKHI couple with the magnetic vortices, leading to resonance between the ions inside the magnetic vortices and Alfvén waves and enhanced ion heating. The induced Alfvén wave resonance results in a broken power-law energy spectrum with a breakpoint at $\sim m_i v_A^2$, where v_A is the Alfvén velocity. We show that the process that forms the nonthermal tail is a second-order Fermi mechanism and the mean spectral index is $\alpha = (1 + 4a^2 D/R)/2$, where D is the spatial scale of the inductive electric field, R is that of vortices, and $a = B_g/B_0$, with ratio of guide field B_g and asymptotic B_0.

Unified Astronomy Thesaurus concepts: Solar flares (1342); Solar magnetic reconnection (1504); Solar energetic particles (1491); Spectral energy distribution (2129)

1. Introduction

Magnetic reconnection (MR) releases magnetic energy through the breaking and reconnecting of oppositely directed magnetic field lines, in the process converting the released magnetic energy into waves and plasma kinetic energy and producing energetic particles and radiation. MR is believed to be responsible for explosive events such as magnetospheric substorms (e.g., Dungey 1961; Galeev et al. 1986; Baker et al. 1996; Zelenyi et al. 2010), solar flares (e.g., Lin 2011; Benz 2017), and possibly X-ray and γ-ray flares from black holes and compact stars (Blandford et al. 2017).

Past studies of particle acceleration in MR concentrated on two types of models. The first is so-called multi-island MR acceleration. In this type of model, particles are accelerated by absorbing the magnetic energy released adiabatically through the contraction of magnetic islands (Drake et al. 2006; Zank et al. 2014; le Roux et al. 2018; Che & Zank 2019). For a model to work, the timescale of magnetic island contraction needs to be long, so that particle motion within the islands can be largely determined by adiabatic invariants. Thus, the acceleration timescale must be comparable to or longer than the reconnection timescale. This implies that the electron acceleration timescale is comparable to the solar flare timescale, contrary to observations that require the acceleration time to be a small fraction of the flare timescale (Vilmer et al. 2011; Benz 2017; Altyntsev et al. 2019). This requirement means that multi-island acceleration is intrinsically inefficient. In particular, ions in principle cannot be accelerated to a power-law energy spectrum in the reconnection timescale. The other type of models involves turbulent acceleration in MR, which can be very efficient (Petrosian 2012). However, what instability can generate the desired turbulence in MR to accelerate particles is unclear (Miller et al. 1996; Grigis & Benz 2006).

Recently, Che & Zank (2020) investigated electron acceleration in a particular type of MR. In force-free current sheets, which are common in the solar corona, the force-free condition $\boldsymbol{j} \times \boldsymbol{B} = 0$ requires an antiparallel component velocity shear in the reconnection plane. As a reconnection event proceeds in the force-free current sheet, the current sheet becomes thinner and the antiparallel velocity shear becomes increasingly intense, which drives an electron Kelvin–Helmholtz instability (EKHI). Che & Zank (2020) discovered that the fast-expanding magnetic vortices generated by the EKHI produce stochastic electric fields, which efficiently accelerate electrons to a power-law energy distribution in a few tens of ion cyclotron periods. The instability also suppresses the Hall effect and generates Sweet–Parker-like electron outflow jets (Che et al. 2021).

In this paper, we present a particle-in-cell (PIC) simulation study of ion acceleration in force-free MR by an EKHI. The simulation domain for the simulation in this paper is larger than in our previous study (Che & Zank 2020; Che et al. 2021) so that the magnetic vortices generated by the EKHI can grow to a few tens of ion inertial lengths. In the simulation, we found that when magnetic vortices expand to sizes comparable to the ion gyroradius, the ions are mildly accelerated. The collisions and mergers of magnetic vortices generate Alfvén waves, which couple with the EKHI turbulence and increase ion heating at the late stage of the simulation. The induced Alfvén wave resonance leads to a broken power-law energy spectrum with a breakpoint at $\sim m_i v_A^2$, where v_A is the Alfvén velocity. The tail of the ion energy spectrum is a power law $f(W_i) \propto W_i^{-\alpha}$ (W_i is the ion kinetic energy). We show that the ion acceleration mechanism is a second-order Fermi process, and that the mean

spectral index depends on the ratio of the spatial scales of the inductive electric field D and that of the vortices R, e.g., $\alpha \approx (1 + 26D/R)/2$. Compared to electrons, we find that: (1) the acceleration of ions is delayed by ∼20 ion cyclotron periods and the acceleration timescale is doubled, and (2) that ions are gradually accelerated to a power-law energy spectrum, while electrons display a two-stage evolution.

The paper is organized as follows. In Section 2, we present the simulation setup and the main results. In Section 3, we examine how an EKHI accelerates ions to form a power-law distribution. We discuss the results in Section 4.

2. Simulation and Results

2.1. The Simulation Model

Using the *p3d* code (Zeiler et al. 2002), we conduct 2D space and 3D momentum PIC MR simulations of double force-free current sheets. While we are only interested in particle acceleration associated with one current sheet, the double current sheet ensures that the same periodic boundary condition in y can be applied. The upper and lower current sheets evolve in the same manner, and we only present results from one of them. The simulation domain has dimensions $L_x \times L_y = 128d_i \times 64d_i$ with grid number 16384×4096. The domain size in the y-direction is twice as large as that in Che & Zank (2020), allowing magnetic vortices to grow sufficiently large and thus allowing more time and space for ions to accelerate. The particle number per cell is 100 for each species.

A force-free current sheet with uniform density and temperature is initialized. Initially, the velocity distribution functions of both electrons and ions are isotropic drifting Maxwellians with temperatures $T_{e0} = T_{i0}$. Both ion and electron current densities are determined by the force-free conditions $\boldsymbol{j}_s \times \boldsymbol{B} = 0$, where s represents particle species, and $\nabla \times \boldsymbol{B} = \boldsymbol{j}$. The initial magnetic field is $B_x/B_0 = \tanh[(y - L_y/2)/w_0]$, where B_0 is the amplitude of asymptotic antiparallel magnetic field B_x and w_0 is the half-width of the initial current sheet. The out-of-plane magnetic field $B_z^2 = B^2 - B_x^2$ is chosen so that the total magnetic field amplitude $|B|$ is constant. At the midplane of the current sheet, $B_x = 0$ and the guide field is defined as $B_g = |B| \neq 0$. In the simulation, we chose $w_0 = 0.5d_i$ and $B_g = 2.5B_0$, where $d_i \equiv c/\omega_{pi}$ and $\omega_{pi,0}$ is the initial ion plasma frequency. The force-free condition requires $j_{s,x} = j_{s,z}B_x/B_z$ being nonzero and follows the sign of the antiparallel B_x within the current sheet. This initialization is in a stable two-fluid force-free equilibrium and a good approximate kinetic equilibrium for low-β plasma.

The plasma $\beta = 0.04$ and the mass ratio is $m_i/m_e = 100$. The ratio of the initial electron plasma frequency $\omega_{pe,0}$ to the initial asymptotic electron gyrofrequency is 2. In the simulation, the mass is normalized to m_i and the temperature is normalized to $m_i v_{A0}^2$ ($v_{A0} = B_0/(4\pi n_0 m_i)^{1/2}$ is the asymptotic ion Alfvén wave speed). The velocity is normalized to v_{A0}, the density to the asymptotic density n_0, the magnetic field to B_0, and the electric field to $E_0 = v_{A0}B_0/c$. The time unit is Ω_i^{-1}, where the asymptotic ion gyrofrequency $\Omega_i = eB_0/m_i c$.

Following the well-tested technique to trigger MR in PIC simulations (Zeiler et al. 2002), a small initial perturbation is applied so that MR occurs. A primary x-line is located at $x = L_x/4 = 32d_i$ and an island is centered at $x = 3L_x/4 = 96d_i$ in the upper current sheet. Instead, a primary x-line at $x = \frac{3}{4}L_x = 96d_i$ and an island at $x = L_x/4 = 32d_i$ are initialized in the lower current sheet such that the periodic boundary condition can be satisfied. The total simulation time is $\Omega_i t = 120$.

2.2. The Development of the EKHI

Around $\Omega_i t = 15$, the current sheet near the x-point of the reconnection contracts to a width close to the electron inertial length ($d_e = \sqrt{m_e/m_i}\,d_i = 0.1d_i$ in our simulation). The antiparallel velocity shear in the x-direction stored in the current sheet drives an EKHI, and magnetic vortices start to emerge with sizes similar to d_e, while a thin and long magnetic island develops on the right side of the domain. As MR proceeds, the magnetic vortices expand and the growth rate of the EKHI decreases. The EKHI enters the nonlinear stage at $\Omega_i t \sim 20$. In Figure 1, we show the velocities in the x-direction for both electrons and ions in the current sheet at different times. At $\Omega_i t = 40$, the average size of the magnetic vortices reaches the ion inertial length d_i and continues to grow to $\sim 5d_i$ at $\Omega_i t = 90$, comparable to the size of the magnetic island, and the magnetic vortices start to interact with the magnetic island. As we have shown in Che et al. (2021), the turbulence suppresses the Hall effect and produces elongated electron and ion jets, which are frozen-in and form Sweet–Parker-like magnetic exhausts. The outflow jets inherit the antiparallel velocity shear of the force-free current sheet and trigger new EKHIs inside the magnetic island (del Sarto et al. 2003; Grasso et al. 2007). Gradually, the magnetic vortices interact with each other and merge. At $\Omega_i t = 120$, the magnetic vortices grow to $\sim 10d_i$ and the coalescence of vortices leads to a significant reduction of the number of magnetic vortices at the left side of the current sheet. The merging of vortices inside the magnetic island leads to the volume of the magnetic island becoming much larger than that of the magnetic vortices. Eventually, except for the vortex at $x = 30d_i$, all other magnetic vortices amalgamate into one and collide with the magnetic island.

2.3. Particle Acceleration and Heating

During the growth of the EKHI, both electrons and ions are accelerated, but the ion acceleration lags the electrons by about $20\Omega_i^{-1}$, which is approximately the time for a vortex to expand from d_e to d_i, implying that the time lag may be longer for the real mass ratio due to $d_i/d_e = (m_i/m_e)^{1/2}$. The time lag is nearly as long as the nonlinear growth stage of the EKHI, during which the ion dynamics are less important and electron dynamics govern. The evolution of the energy spectra of ions and electrons also appears to be different, and the ion acceleration is delayed by a similar time lag, suggesting the ions experienced a different acceleration process from that of the electrons.

In Figure 2, we show both the electron and ion energy spectra as a function $\gamma - 1$ at different times, where γ is the Lorentz factor defined as $\gamma = 1/(1 - v^2/c^2)^{1/2}$. At $\Omega_i t \sim 16$, the electron energy spectrum becomes a power law in the form of $f \propto (1 - \gamma)^{-\alpha}$ above $\gamma - 1 = 0.1$ with index $\alpha \sim 4.8$. At $\Omega_i t \sim 64$, the acceleration saturates and a harder spectrum with $\alpha \sim 3.4$ above $\gamma - 1 = 0.2$ is formed, exhibiting a softer–hard–harder two-stage evolution. This corresponds to the linear and nonlinear growth stages of the EKHI, similar to what has been found previously (Che & Zank 2020). On the other hand, the energy spectrum of ions gradually reaches a power law near the end of the simulation at $\Omega_i t \sim 112$ and the acceleration time is about two times longer than that of the electrons. An outstanding feature of the final ion energy spectrum is a broken

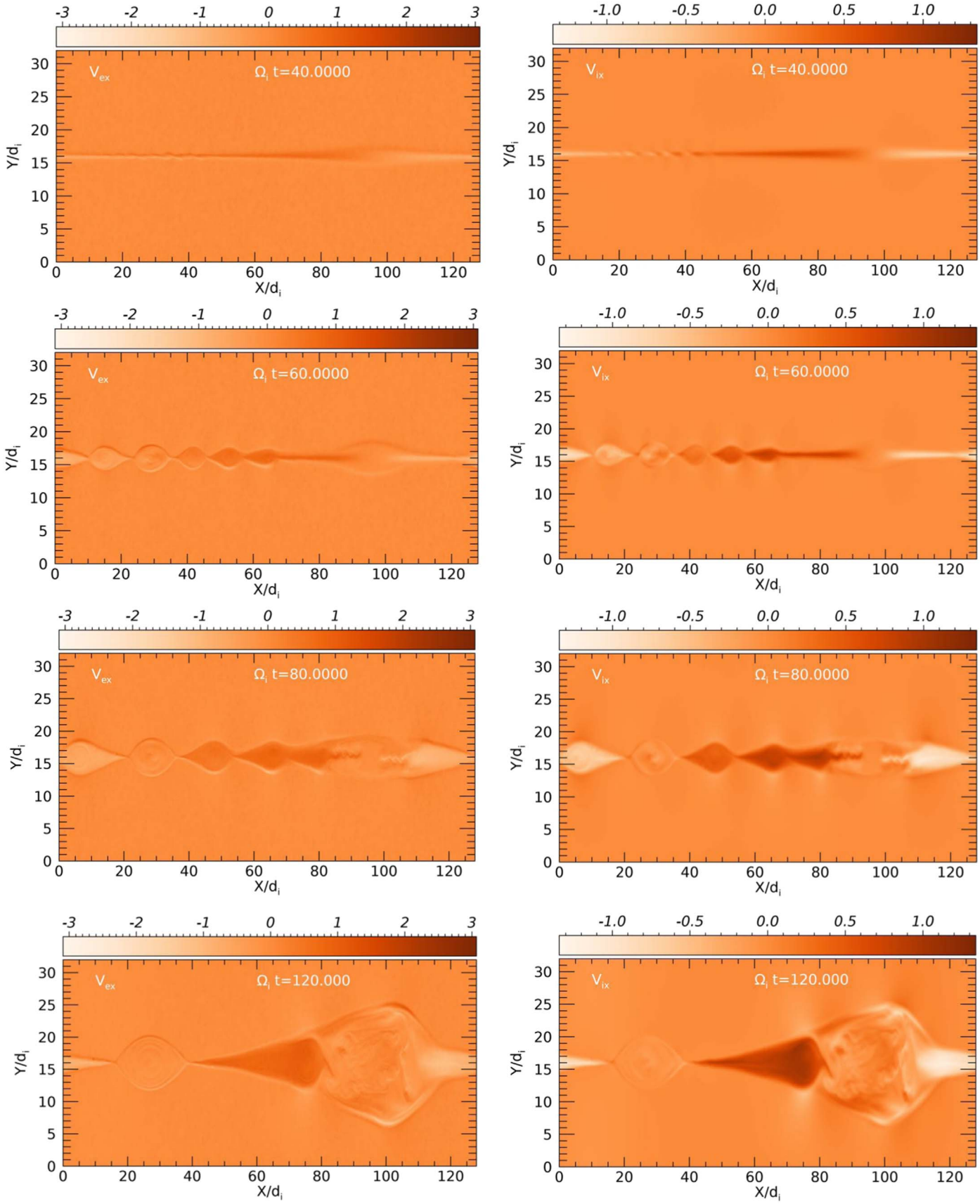

Figure 1. Electron velocities v_{ex} (left panels) and ion velocities v_{ix} (right panels) in the x-direction at $\Omega_i t = 40$, 60, 80, and 120.

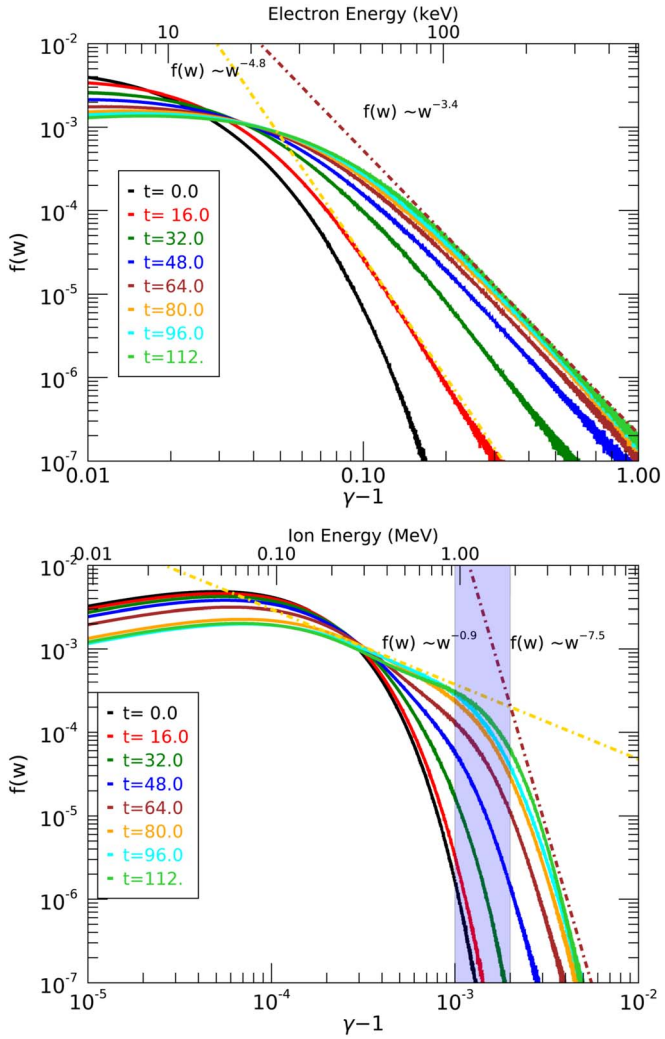

Figure 2. Top panel: electron energy spectra. Bottom panel: ion energy spectra. The shaded area marks the knee of the broken power law.

power law with the indices $\alpha_1 = 0.9$ below and $\alpha_2 = 7.5$ above the turning point at $\gamma - 1 \sim 1.5 \times 10^{-3}$.

In Figure 3, we further show the ion velocity distribution functions at different times. At $\Omega_i t \geqslant 64$, a significant plasma heating occurs in the x-direction, while the plasma heating in y and z is much weaker. Two distinct bumps around $\pm v_{A0}$ can be seen in the x-direction velocity distribution functions at $\Omega_i t = 80$, 96, and 112, indicating the resonant damping of Alfvén waves propagating in both positive and negative x-directions.

In Figure 4 (top panel), we show the spatial–temporal power density spectrum of B_y along x at the midplane of the current sheet at $\Omega_i t = 64$–112. Waves can be seen propagating in both directions with the phase speed of the Alfvén wave, with a peak at frequency $\omega \ll \Omega_i$ and wavenumber $k_x d_i \ll 1$, showing the waves are indeed Alfvén waves, satisfying the shear Alfvén wave dispersion relation $\omega = k_x v_A$. The generation of Alfvén waves is a natural consequence of the coalescence of magnetic vortices that produce intense magnetic field perturbations of B_y on spatial scales of a few tens of d_i along the x- and y-directions. To explicitly show the correlation between the magnetic vortices and the generation of Alfvén waves, we show the stack of the slices of B_y along x at the midplane of the current sheet from $\Omega_i t = 40$–120 in Figure 4 (bottom panel). At

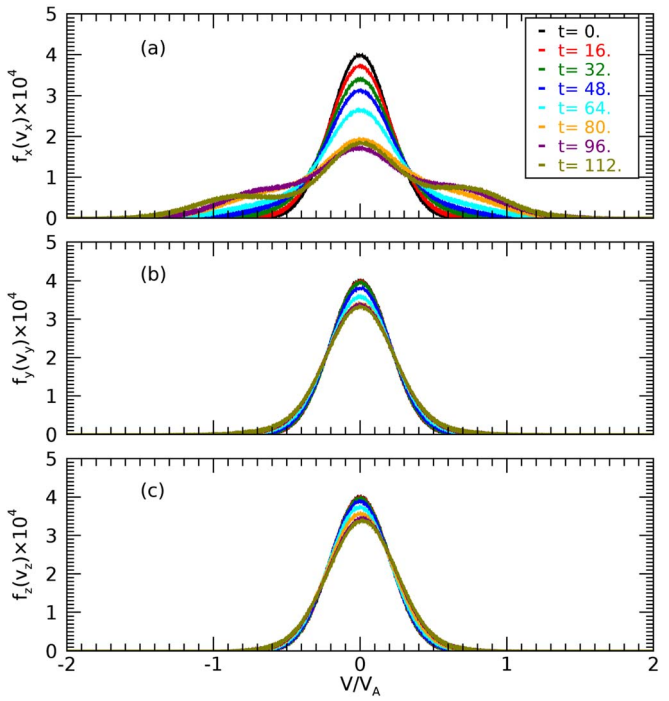

Figure 3. Ion velocity distributions (a) $f(v_x)$, (b) $f(v_y)$, and (c) $f(v_z)$ at different times. The velocity is normalized to the initial Alfvén velocity.

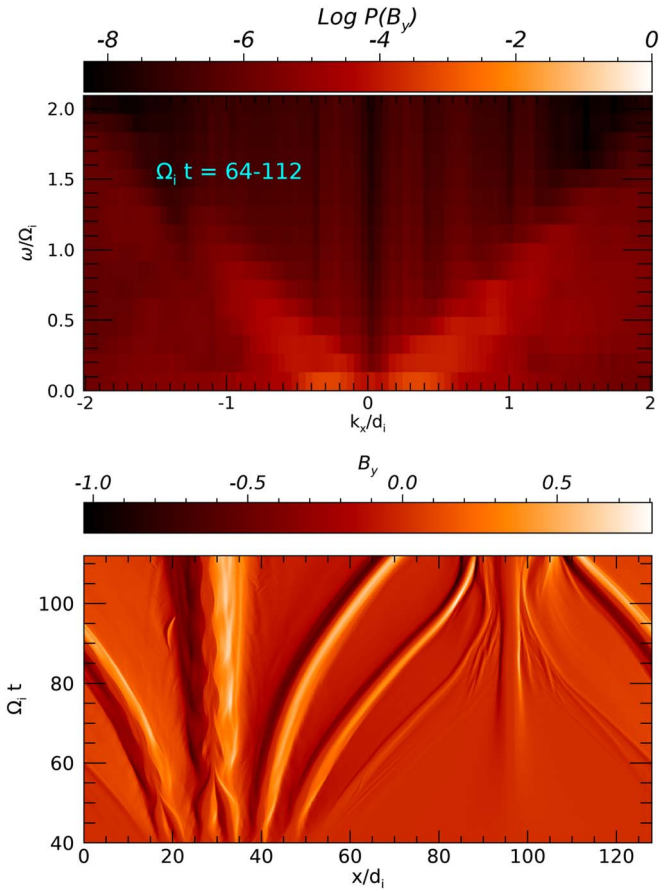

Figure 4. Top panel: The $\omega/\Omega_i - k_x/d_i$ diagram of B_y fluctuations propagating along x at the midplane of the current sheet. The data are from $\Omega_i t = 64$–112. Bottom panel: The stack of the cuts of B_y along x at the midplane of the current sheet.

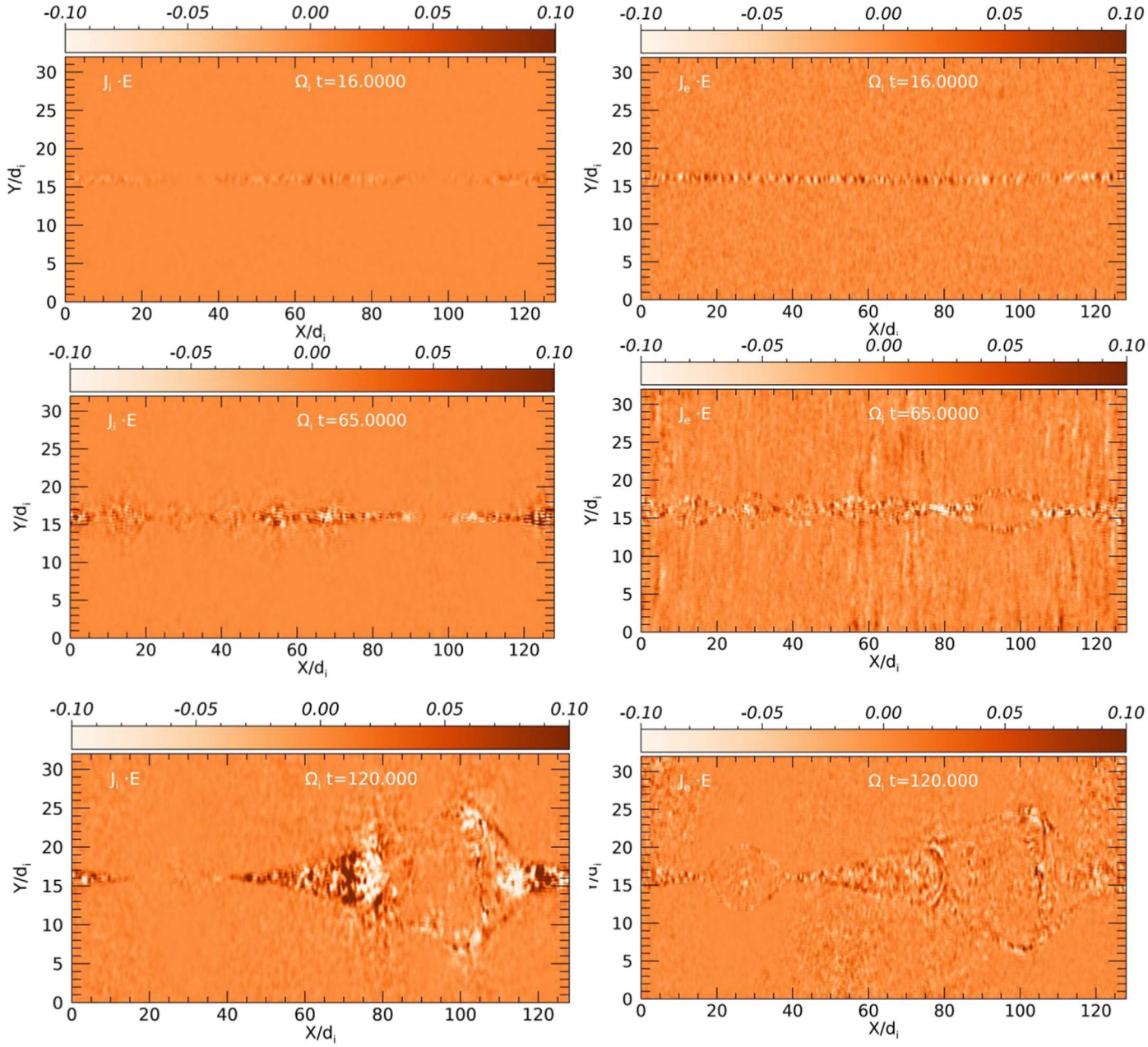

Figure 5. The ion heating $\boldsymbol{j}_i \cdot \boldsymbol{E}$ (left) and electron heating $\boldsymbol{j}_e \cdot \boldsymbol{E}$ (right) at $\Omega_i t = 16$, 65, and 120.

$x \sim 30d_i$, the location of the initial x-point of MR, two vortices collide and merge into a larger and nearly motionless vortex that keeps expanding. The neighboring magnetic vortices, on the other hand, move either forward or backward. Eventually, they all reach the center of the magnetic island at $x = 100d_i$ and drive into the magnetic vortices generated by the outflow jets in the elongated magnetic exhaust. In Figure 1, we show that both v_{ex} and v_{ix} increase as MR proceeds. As a result, the drift speeds of the magnetic vortices along x also gradually increase to the Alfvén wave phase speed v_{A0}, indicating a resonance between the EKHI and the Alfvén waves, which causes the ion energization. In our previous study (Che et al. 2021), we found that the drift of the particles along the x-direction satisfies the frozen-in condition that guarantees the generation of Alfvén waves rather than kinetic waves.

To better understand the ion energization, we show $\boldsymbol{j}_s \cdot \boldsymbol{E}$ for both ions and electrons (s indicates the particle species) in Figure 5. At $\Omega_i t = 16$, the size of vortices is about a few d_e, and the electron energization is strong. The first stage of the acceleration has passed and a power-law energy spectrum with index $\alpha = 4.8$ is formed, as shown in Figure 2. On the other hand, the ion energization at this time is weaker. The ion gyroradius is $r_{Li} = 2\pi v_{t,i}/\Omega_i \sim 1.2d_i \sim 12d_e$, where the ion initial temperature $m_i v_{t,i}^2 = T_i = 0.04$ and, for a mass ratio of 100, $d_i/d_e = 10$. For efficient ion acceleration, the size of the vortices must be larger than $1.2d_i$, which is reached at $\Omega_i t \sim 40$ (see Figure 1). At this time, $\boldsymbol{j}_e \cdot \boldsymbol{E}$ and $\boldsymbol{j}_i \cdot \boldsymbol{E}$ are comparable. At $\Omega_i t = 65$ and 120, the ion energization becomes stronger than that of the electrons, since the electrons cannot efficiently interact with low frequency waves. The expansion of magnetic

vortices also leads to a decrease of magnetic field strength and weaker inductive electric field, which should make particle acceleration weaker. However, $\boldsymbol{j}_i \cdot \boldsymbol{E}$ remains at about the same level at the late stage of the EKHI, which indicates that another new acceleration process should be present. This is where the Alfvén waves shown in Figure 4 play an important role. These counterpropagating waves resonate with the ions in the EKHI vortices that travel at $v_x \sim v_A$ in the exhaust and enhance the ion acceleration. For the stationary vortex at $x = 30d_i$, there is no Alfvénic resonance; hence, the ion energization at the late stage is very weak. In the magnetic island, electrons and ions only start to be accelerated when the outflow jets drive a secondary EKHI in the island, at $\Omega_i t \sim 80$.

The resonance between the EKHI and Alfvén waves helps ions trapped inside magnetic vortices to experience two energization processes simultaneously. One is acceleration by the stochastic electric field, induced by the expansion of the magnetic vortices. Similar to electron acceleration, this process produces a power-law energy spectrum. The other is the Alfvén wave turbulence that generates strong ion heating due to the stochastic motion in magnetic turbulence (Hasegawa & Chen 1974; Chen & Hasegawa 1974; Schlickeiser 1989; Escande et al. 2019), which gives a strong boost to the energy spectrum around $m_i v_{A0}^2/2$, the corresponding $\gamma - 1 \sim 1.3 \times 10^{-3}$ as shown in Figure 2. The heating leads to a plateau at $\gamma - 1 \sim 1.3 \times 10^{-3}$ and the power-law tail above that in the ion energy distribution, resulting in a broken power law.

3. EKHI and the Ion Energy Power Law

In the preceding section, we have shown that the resonant Alfvén wave heating contributes to the ion acceleration and determines the lower-energy power law. The high-energy tail with power-law index 7.8, on the other hand, is produced by the EKHI. Following the analysis of electron acceleration in Che & Zank (2020), we show that ion acceleration is also a second-order Fermi process, and we estimate the high-energy power-law index and compare with the simulation.

When magnetic vortices expand to a size larger than the ion gyroradius r_{Li} at $\Omega_i t \sim 40$, where $r_{Li} = 2\pi v_{t,i}/\Omega_i \sim 1.2d_i$, the EKHI is already in the middle of the nonlinear stage and the growth of magnetic vortices is slow. The timescale of magnetic field variation τ_{gi} is much longer than the ion gyroperiod $\tau_g \gg \Omega_i^{-1}$. From $\Omega_i t = 40$–120, the average size of magnetic vortices increases from $\sim 1d_i$ to $\sim 8d_i$, leading to a decrease of magnetic field $\boldsymbol{B}_{ip} = B_x\hat{x} + B_y\hat{y}$ in the reconnection plane xy. Using $\partial B_{ip}/\partial t \sim B_{ip}/\tau_{gi}$, we have $\tau_{gi} \sim 10\Omega_i^{-1}$. The expansion of magnetic vortices induces stochastic electric fields E_z via Faraday's law $\nabla \times \boldsymbol{E} = -\frac{1}{c}\partial \boldsymbol{B}_{ip}/\partial t$. The inductive electric field E_z accelerates the ions to a power-law energy spectrum.

Following Che & Zank (2020), we can write the mean acceleration rate of $v_{z,i}$ over one ion gyroperiod $T = 2\pi\Omega_i^{-1}$

$$\frac{\delta v_{z,i}}{\delta t} = \frac{\cos^2\theta}{2\tau_{gi}} v_{z,i}, \tag{1}$$

where $\cos\theta = \hat{b} \cdot \hat{b}_{ip}$, $\hat{b} = \boldsymbol{B}/B$, and $\hat{b}_{ip} = \boldsymbol{B}_{ip}/B_{ip}$. We can approximate $\cos\theta \sim v_{L,i}/v_{z,i}$, where $v_{L,i} \sim v_{t,i}$, and $v_{z,i}$ is the velocity of energetic tail ions. This is different from the electrons whose $v_z \sim c$, $v_{z,i} \ll c$, but $v_{z,i} \gg v_{t,i}$. Thus, we still have $\cos^2\theta \ll 1$, indicating that this is still a second-order Fermi acceleration.

Similarly, we can show that the ion energy power-law index is related to the guide field and magnetic vortices via

$$f_{z,i}(W_{z,i}) \propto W_{z,i}^{-(1+4a^2\frac{D}{R})/2}, \tag{2}$$

where $a = B_g/B_0$ and B_g is the guide field. In this simulation, $a = 2.5$, D is the characteristic spatial scale of the inductive electric field, and R is the spatial scale of magnetic vortices.

With Equation (2), we can estimate the saturation index of the ion power-law energy spectrum. The ratio of electric field variation and the size of magnetic vortices D/R can be roughly obtained from Figure 5, since ion heating follows the electric field (it does not make much difference if we look at the variation of electric field directly). At $\Omega_i t \sim 65$, the electron energy power-law spectrum becomes saturated with $\alpha = 3.4$, while the ion heating just starts. From Figure 5, we can see $D/R \sim 1/4$ and hence the index $\alpha = 3.6$ from Equation (2), consistent with what we obtained from the energy spectrum shown in Figure 2. The ion energy spectrum does not become a power law until the end of the simulation. At $\Omega_i t = 120$, the electron heating has ceased due to inefficient coupling with low frequency waves. From Figure 5, we estimate the ratio of $D/R \sim 1/2$, which gives an index 7.3, consistent with $\alpha \sim 7.5$ in the ion energy spectrum in Figure 2.

4. Discussion and Conclusion

Mildly relativistic particle acceleration in MR is a multiscale problem. In principle, electron acceleration requires that the turbulent dynamical scale be larger than the electron gyroradius, and ion acceleration requires that the turbulent dynamical spatial scale be larger than the ion gyroradius, so that both particles can be accelerated with sufficient time before leaving the acceleration region. The ratio of the dynamical scales of electrons and ions is proportional to $(m_e/m_i) \ll 1$. Past research on particle acceleration has found that the favored acceleration mechanism is turbulent acceleration, which is efficient and stochastic, satisfying the requirements for the production of power-law distributed energetic particles. The key element in turbulent acceleration is how to generate the needed turbulence on multiscales in MR so that both electrons and ions can be efficiently accelerated (Miller et al. 1996; Grigis & Benz 2006; Petrosian 2012).

This paper uses PIC simulations to demonstrate an example in which both electrons and ions are accelerated to power-law energy distributions efficiently. We show that the EKHI is driven when the width of current sheet reaches the electron inertial length d_e. During MR, EKHI turbulence dominates the Hall effect and produces a Sweet–Parker-like magnetic exhaust filled with electron and ion jets. These jets are frozen-in with the magnetic field and trigger new EKHIs inside the magnetic island at a late stage. As a result, magnetic vortices fill the current sheets and generate a more effective stochastic acceleration. Similarly to what we have shown in our previous work, the electrons are quickly accelerated in less than 20 ion gyroperiods by the stochastic electric field induced by the expansion of the magnetic vortices, and the indices of the energy power spectra harden in a two-stage fashion that corresponds to the linear and the nonlinear development of the EKHI (Che & Zank 2020; Che et al. 2021). In contrast, ion acceleration does not begin until the magnetic vortices have grown to a size larger than the ion gyroradius when electron acceleration nearly saturates. The timescale of in-plane

magnetic field variation is much slower than the ion gyroperiod, leading to weaker stochastic electric fields. Similarly to electrons, ions experience a second-order Fermi acceleration. Besides acceleration by the stochastic electric field from the EKHI, ions are also accelerated by counter-propagating Alfvén wave turbulence generated by the perpendicular magnetic perturbations caused by the EKHI. The resonant coupling between EKHI vortices and the Alfvén waves leads to a break in the ion power-law energy spectrum at $m_i v_{A0}^2$, with a strong enhancement of the lower-energy spectral index. The high-energy tail of the ion energy spectrum satisfies the same formula as that of electrons (Che & Zank 2020) $f_{z,i}(W_{z,i}) \propto W_{z,i}^{-(1+4a^2\frac{D}{R})/2}$, where the index is determined by the guide field $a = B_g/B_0$ and the the ratio of the spatial scales between the electric field and magnetic vortices.

To compare our simulation to observations, we need to convert the Lorentz factor in our simulation to the electron and ion energies. Unfortunately, this is not an easy task because in most PIC simulations, including this one, the mass ratio between ion and electron is chosen to be smaller than the actual ratio, so that meaningful results can be obtained without very costly computations. The mass ratio for this study is 100. A real mass ratio is needed to make the conversion self-consistent. However, it is found that the mass ratio affects the dynamical development weakly when m_i/m_e reaches 100 (Birn et al. 2001). Given this caveat, we assume that our results can be extended to the real mass ratio, and we scale the Lorentz factor with the real rest mass energy, which allows us to compare our results to observations. We show the fiducial energy in Figure 2 using $m_e c^2 = 511$ keV and $m_i c^2 = 938$ MeV. We find that the electrons are accelerated to a few hundreds of keV while the corresponding energy of energetic ions is from hundreds of keV to a few MeV. The energy spectra of electrons is a single power law and the spectral index α evolves from 4.8 to 3.5. As a comparison, the power-law energy spectra of ions is broken at 1 MeV, the index at the lower energy is about 1 while the index at higher energies is much softer, with $\alpha \sim 7.5$. Mildly relativistic energetic ions with power-law spectra have been commonly observed together with energetic electrons in magnetospheric substorms and solar flares (Zelenyi et al. 1990; Emslie et al. 2012; Vilmer 2012; Imada et al. 2015). The in situ particle acceleration observations in the Earth's magnetotail during MR found that most of the electrons are accelerated to about a few hundred keV and some to 1 MeV, with a large spectral index range from 2 to 6 (Baker & Stone 1977; Zhou et al. 2016). Most of the energetic ions are accelerated to tens and even hundreds of keV, and the spectral indices range from 2.5 to 6 (Fan et al. 1975; Baker et al. 1979; Imada et al. 2015). The simulation presented in this paper is consistent with the basic magnetospheric observations of particle energy and the association with MR, though the high-energy tail of the ion spectrum appears softer in our simulation. Solar flare observations suggest that the acceleration of protons is more related to the acceleration of electrons of high energies than to the acceleration of more abundant subrelativistic particles, implying that the turbulence that accelerates electrons in MR is probably the same turbulence that accelerates ions (Vilmer et al. 2011). The γ-ray observations of solar energetic protons with energy above 1 MeV infer a single power-law index in the range of 3–5 and averaging about 4.3 (Ramaty et al. 1996; Murphy et al. 2007; Emslie et al. 2012). Similar to magnetospheric ion acceleration, the ion energy spectrum in our simulation is softer. Observation of solar energetic ions is limited by the minimum energy of 1 MeV, and the energy spectra below 1 MeV are not available from γ-ray observations. Observationally and theoretically, our knowledge of ion acceleration in solar flares is still very limited, and more work is clearly needed. While our estimates appear to agree reasonably well with observations, real mass ratio simulations are needed to confirm these comparisons given the caveats of energy conversion.

The broken power-law ion energy spectrum is one of the interesting features in our simulation. However, for ions, it is hard to use γ-ray observations to detect the energy distribution below 1 MeV, and a full picture of the ion energy distribution is hard to obtain. A few in situ observations of impulsive solar flares by WIND show that ions also demonstrate broken power-law energy spectra, in which the lower energy is flatter and enhanced, indicating Alfvén wave turbulence heating (Reames et al. 1997; Vilmer et al. 2011; Vilmer 2012; Reames 2021).

Since Fermi proposed the first acceleration mechanism in 1949 for the production of highly relativistic cosmic rays with an inverse power-law energy spectrum $f(W) \propto W^{-\alpha}$, the "injection problem" remains one of the outstanding issues in particle acceleration (Fermi 1949). The study of energetic particles produced in the heliosphere with electron energy typically at hundreds of keV (up to MeV) and with ion energy typically at tens of MeV (up to GeV), it is crucial to understand the "injection problem." The simple numerical model has demonstrated a possible way to quickly accelerate ions to a power law together with electrons, but numerous questions regarding turbulence acceleration in MR are still unanswered, and require further investigations.

H.C. is very grateful to Dr. Y. Yang for his help in analyzing the simulations and providing critical comments on the manuscript. H.C. acknowledges partial support by NASA Heliophysics Career award No. 80NSSC19K1106 and HSR program No. NNX17AI19G. H.C. and G.P.Z. acknowledge the partial support of an NSF EPSCoR RII-Track-1 Cooperative Agreement OIA-1655280. G.P.Z. acknowledges partial support from an NSF/DOE Partnership in Basic Plasma Science and Engineering via NSF grant PHY-1707247. The simulations were supported by the NASA High-End Computing (HEC) Program through the NASA Advanced Supercomputing (NAS) Division at Ames Research Center.

ORCID iDs

H. Che https://orcid.org/0000-0002-2240-6728
G. P. Zank https://orcid.org/0000-0002-4642-6192
A. O. Benz https://orcid.org/0000-0001-9777-9177

References

Altyntsev, A. T., Meshalkina, N. S., Lysenko, A. L., & Fleishman, G. D. 2019, ApJ, 883, 38
Baker, D. N., Belian, R. D., Higbie, P. R., & Hones, E. W. 1979, J, JGR, 84, 7138
Baker, D. N., Pulkkinen, T. I., Angelopoulos, V., Baumjohann, W., & McPherron, R. L. 1996, JGRA, 101, 12975
Baker, D. N., & Stone, E. C. 1977, JGR, 82, 1532
Benz, A. O. 2017, LRSP, 14, 2
Birn, J., Drake, J. F., Shay, M. A., et al. 2001, JGR, 106, 3715
Blandford, R., Yuan, Y., Hoshino, M., & Sironi, L. 2017, SSRv, 207, 291
Che, H., & Zank, G. P. 2019, JPhCS, 1332, 012003
Che, H., & Zank, G. P. 2020, ApJ, 889, 11

Che, H., Zank, G. P., Benz, A. O., Tang, B., & Crawford, C. 2021, ApJ, 908, 72
Chen, L., & Hasegawa, A. 1974, PhFl, 17, 1399
del Sarto, D., Califano, F., & Pegoraro, F. 2003, PhRvL, 91, 235001
Drake, J. F., Swisdak, M., Che, H., & Shay, M. A. 2006, Natur, 443, 553
Dungey, J. W. 1961, PhRvL, 6, 47
Emslie, A. G., Dennis, B. R., Shih, A. Y., et al. 2012, ApJ, 759, 71
Escande, D. F., Gondret, V., & Sattin, F. 2019, NatSR, 9, 14274
Fan, C. Y., Gloeckler, G., & Hovestadt, D. 1975, PhRvL, 34, 495
Fermi, E. 1949, PhRv, 75, 1169
Galeev, A. A., Kuznetsova, M. M., & Zelenyi, L. M. 1986, SSRv, 44, 1
Grasso, D., Borgogno, D., & Pegoraro, F. 2007, PhPl, 14, 055703
Grigis, P. C., & Benz, A. O. 2006, A&A, 458, 641
Hasegawa, A., & Chen, L. 1974, PhRvL, 32, 454
Imada, S., Hirai, M., & Hoshino, M. 2015, EP&S, 67, 203
le Roux, J. A., Zank, G. P., & Khabarova, O. V. 2018, ApJ, 864, 158
Lin, R. P. 2011, SSRv, 159, 421
Miller, J. A., Larosa, T. N., & Moore, R. L. 1996, ApJ, 461, 445
Murphy, R. J., Kozlovsky, B., Share, G. H., Hua, X. M., & Lingenfelter, R. E. 2007, ApJS, 168, 167
Petrosian, V. 2012, SSRv, 173, 535
Ramaty, R., Mandzhavidze, N., & Kozlovsky, B. 1996, in AIP Conf. Ser., 374, High Energy Solar Physics, ed. R. Ramaty, N. Mandzhavidze, & X.-M. Hua (NY: Melville), 172
Reames, D. V. 2021, Solar Energetic Particles. A Modern Primer on Understanding Sources, Acceleration and Propagation, Vol. 978 (Cham: Springer)
Reames, D. V., Barbier, L. M., Von, Rosenvinge, et al. 1997, ApJ, 483, 515
Schlickeiser, R. 1989, ApJ, 336, 243
Vilmer, N. 2012, RSPTA, 370, 3241
Vilmer, N., MacKinnon, A. L., & Hurford, G. J. 2011, SSRv, 159, 167
Zank, G. P., le Roux, J. A., Webb, G. M., Dosch, A., & Khabarova, O. 2014, ApJ, 797, 28
Zeiler, A., Biskamp, D., Drake, J. F., et al. 2002, JGR, 107, 1230
Zelenyi, L. M., Artemyev, A. V., Malova, K. V., Petrukovich, A. A., & Nakamura, R. 2010, PhyU, 53, 933
Zelenyi, L. M., Lominadze, J. G., & Taktakishvili, A. L. 1990, JGR, 95, 3883
Zhou, M., Li, T., Deng, X., et al. 2016, JGRA, 121, 3108